Wolff, Franziska; Lotsari, Eliisa; Spieler, Diana; Elias, Melanie; Eltner, Anette

Enhancement of two-dimensional hydrodynamic modelling based on UAV- flow velocity data

Published in:
Earth Surface Processes and Landforms

DOI:
10.1002/esp.5853

Published: 01/07/2024

Document Version
Publisher's PDF, also known as Version of record

Please cite the original version:
Wolff, F., Lotsari, E., Spieler, D., Elias, M., & Eltner, A. (2024). Enhancement of two-dimensional hydrodynamic modelling based on UAV- flow velocity data. *Earth Surface Processes and Landforms*, *49*(9), 2736-2750.
https://doi.org/10.1002/esp.5853

Received: 2 March 2023 | Revised: 29 February 2024 | Accepted: 7 April 2024

DOI: 10.1002/esp.5853

RESEARCH ARTICLE

ESPL WILEY

Enhancement of two-dimensional hydrodynamic modelling based on UAV- flow velocity data

Franziska Wolff[1] | Eliisa Lotsari[1,2] | Diana Spieler[3] | Melanie Elias[4] | Anette Eltner[4]

[1]Department of Geographical and Historical Studies, University of Eastern Finland, Joensuu, Finland

[2]Department of Built Environment, Water and Environmental Engineering, Aalto University, Aalto, Finland

[3]Institute of Hydrology and Meteorology, TUD Dresden University of Technology, Dresden, Germany

[4]Institute of Photogrammetry and Remote Sensing, TUD Dresden University of Technology, Dresden, Germany

Correspondence
Franziska WOLFF, Department of Geographical and Historical Studies, University of Eastern Finland, Joensuu 80101, Finland.
Email: franziska.wolff@uef.fi

Funding information
Research Council of Finland; Deutscher Akademischer Austauschdienst, Grant/Award Number: 332563; Academy of Finland, Grant/Award Numbers: 337394, 338480; University of Eastern Finland; Aalto University

Abstract

2D hydrodynamic models deepen the understanding of hydromorphological processes in fluvial systems. UAV (Unoccupied Aerial Vehicles) can record complementary calibration and validation data for these models of large areas. In this study, we created a 2D hydrodynamic model of the Pulmanki River in Northern Finland under shallow, open-channel conditions based on three calibration sets. We examined the potential of UAV-flow velocities for model validation. Here, we applied a cross-validation approach comprising the conversion from surface to depth-averaged velocity and vice versa using fixed velocity coefficients (α). We further assessed the conversion performance including hydraulic variables to evaluate this coupled numerical-experimental concept. Our model showed good performance in the three calibration runs for water level and depth-averaged velocity. The calculation of surface to depth-averaged velocity identified the coefficient $\alpha = 0.8$ as the best choice with $R^2 = 0.62$ for the straight river reach, indicating a good agreement between converted velocity and the reference data. A poor agreement, however, is evident for the meander section with $R^2 = 0.406$. While there were no statistically significant relationships between the conversion performance and hydraulic variables, there were observable trends in the residuals indicating over- and underestimation of converted velocities, particularly in relation to bathymetry and distance to the channel centre, with variations based on the river structure. Our study demonstrates that UAV reference data has the potential to enhance 2D hydrodynamic models but particularly improves our understanding of spatial flow distribution.

KEYWORDS
computational fluid dynamics, depth-averaged velocity, PTV-method, surface velocity, velocity coefficient

1 | INTRODUCTION

Hydrodynamic modelling can provide meaningful scenarios for water resources management and allow the assessment of interactions between hydromorphological processes and landforms (Blanckaert, 2018; Mosselman, 2005). Increasing the modelling accuracy and capacity over larger areas promotes the knowledge of ongoing dynamics, which is particularly important for the prediction of events with extreme magnitude, i.e., flash floods. The calibration and validation of the models is based on a variety of spatially and temporally representative data sets. Thus, accurate field measurements are a prerequisite to apply these models with confidence. Measurements usually conducted with traditional devices such as ADCP (Acoustic Doppler Current Profiler) for velocity measurements and Laser scanners or RTK-GNSS systems (Realtime Kinematic Global Navigation SatelliteSystem) to acquire topography data (Lotsari et al., 2017; Lotsari, Thorndycraft, & Alho, 2015; Polvi et al., 2020; Vaaja et al., 2011). The standard calibration and validation use among others observed water levels (WL) and the adjustment of the roughness values (n) of the selected models (Hunter et al., 2007; Lane et al., 2005). As hydrodynamic models incorporate processes such as secondary shear stress, which may not be directly measurable, calibration becomes a crucial step. The modelled velocity, however, is a more complicated parameter to validate correctly for these numerical models (Kasvi et al., 2015). This is due to the higher spatial and temporal variability of the flow velocity conditions, which may vary over short distances. Pulses of higher and lower flow exist within natural open-channel conditions (Lotsari, Dietze, et al., 2020). While this demands spatially dense measurements, often the velocities are only measured at cross-sections or as single point-measurements. Therefore, there is a need for spatially representative velocity data to calibrate and validate the models and to understand the hydraulics of the river channel.

This is especially important when using 2D models, as these are often selected for scientific and practical engineering purposes because of the fewer amount of data needed for their calibration and validation compared with 3D models. Both models calculate depth-averaged velocity (DAV), which is especially effective for capturing spatial variations in flow, particularly in meandering or braided river reaches. They require, however, high spatial resolution information of land surface topography as input to model flow velocity accurately. During the creation of the model and the simulation area, these are interpolated on a grid established to represent the simulation area. The grid resolution depends on the simulation purpose, however, the finer the resolution the higher the computation time. Thus, a grid with coarse resolution would be preferable under the premise that the model can still represent spatial variations and dynamics of flow velocities (Detert et al., 2017; Dietrich, 2017; Eltner et al., 2021; Kasvi et al., 2019; Woodget et al., 2014).

Given the demand for spatially explicit models, remote sensing platforms can collect reference data, such as bathymetry and topography, covering larger geographic areas (Eltner et al., 2021; Langhammer et al., 2017; Masafu et al., 2022). A recent publication by Masafu et al. (2022) shows that UAVs (unmanned aerial vehicles, such as drones) may become a solution for spatially varying velocity data. The concepts of UAV-reference data rely on Structure from Motion (SfM) photogrammetry and velocimetry techniques, namely particle tracking velocimetry (PTV), large-scale particle-image velocimetry (LSPIV), and Space–time image velocimetry (STIV) providing elevation and surface velocity (SV) data. Methods focusing on the tracking of particles have been used in many studies to derive SV (Brauneck et al., 2019; Eltner, Hoffmeister, et al., 2020; Fujita et al., 2007; Masafu et al., 2022; Muste et al., 2011). However, the use of UAVs for acquiring fluvial data in the calibration and validation process for hydrodynamic modelling is still in its early stages.

There needs to be a systematic way of converting and comparing velocities from a 2D model and UAV measurements (Biggs et al., 2023). This involves testing conversion coefficients (Masafu et al., 2022) and evaluating how various hydraulic factors impact the accuracy of the model and the conversion of velocities. Previous studies have linked the complexity of the coefficient determination to variations in hydraulic radius and channel roughness (Genç et al., 2015; Hauet et al., 2018; Le Coz et al., 2010; Rantz, 1982). Opting for a fixed coefficient for a specific study site presents the simplest and quickest model validation approach, but it prompts questions about the acceptable deviation between modelled and calculated velocities and how to define this tolerance. To our knowledge, model validation based on UAV surface velocities has been done only for a temperate, restored meandering river reach with gravel bed material, and therein from surface velocity to depth-averaged velocity (Masafu et al., 2022). Hence, it is necessary to conduct analyses on additional river systems, including both natural and human-impacted ones, to assess the broader applicability of this data. Moreover, the advantage of UAV-data is not only to generate SVs but also to use different spatial datasets for the assessment of velocity conversion and model performance. This can be done by deriving UAV-based bathymetry and channel information.

This study hypothesizes that the multifaceted benefits of utilizing UAV-data in the calibration and validation process enhances the model's ability to match observed river flow conditions and the understanding of flow dynamics. To manifest this, we conduct a cross-validation to assess the empirical velocity conversion's performance. This involved comparing numerical model predictions with experimentally derived results of fixed velocity coefficients and their relation to hydraulic variables. If UAV-data can indeed improve the modelling processes, it would enable hydrodynamic modelling and even sediment transport analyses of larger and remote river segments in situations where measurements would be otherwise difficult or risky, such as high flow conditions or wide flooding situations. The aims of this study are therefore to 1) enhance field measurement approaches by integrating UAV reference datasets for 2D hydrodynamic modelling, and 2) to investigate the use of fixed coefficients (α) for velocity conversions in a cross-validation process. The approach is tested under shallow, open-channel flow conditions of a sandy meandering river within the outback area of Finnish Lapland.

2 | STUDY SITE

Our study site is situated at the upper Pulmanki River in Northern Finland and is a tributary to Lake Pulmanki, which further drains into the Tana River forming the Finnish-Norwegian border. Characteristic to the river channel are meander bends with distinct, erodible banks up to 19 m, a grain size of 0.05–0.45 mm (Lotsari, Dietze, et al., 2020) and clear, vegetation-poor water. The present-day river incises unconsolidated deposits of glacio-lacustrine and -fluvial sediment (Hirvas et al., 1988). The elevation gradient between land surface and river channel is partly steep having 35–36° friction angles in some reaches (Lotsari, Hackney, et al., 2020). Located in the polar region, the river is characterized by floods arising from spring snow melt and rain causing heavy erosion, sedimentation and overall sediment transport of bank, point-bar and mid-channel bar materials. The discharges vary from 0.61 m^3 s^{-1} in mid-winter conditions (Lotsari, Dietze, et al., 2020) to 72 m^3 s^{-1} measured in spring 2017 (Lotsari, Hackney, et al., 2020). The study area was selected to represent flow conditions both within a straight river reach and within a symmetrical meander bend with high curvature (sinuosity 1.5; cf. Bend number 6 of Lotsari et al., 2014) that follows the straight section. The study area represents the simulation area for the hydrodynamic model and covers a river segment of ca. 1.4 km including two selected area of interests (AOI) in a straight and meandering section. Fieldwork data is accessible across the entire reach and within the AOIs (Figure 1).

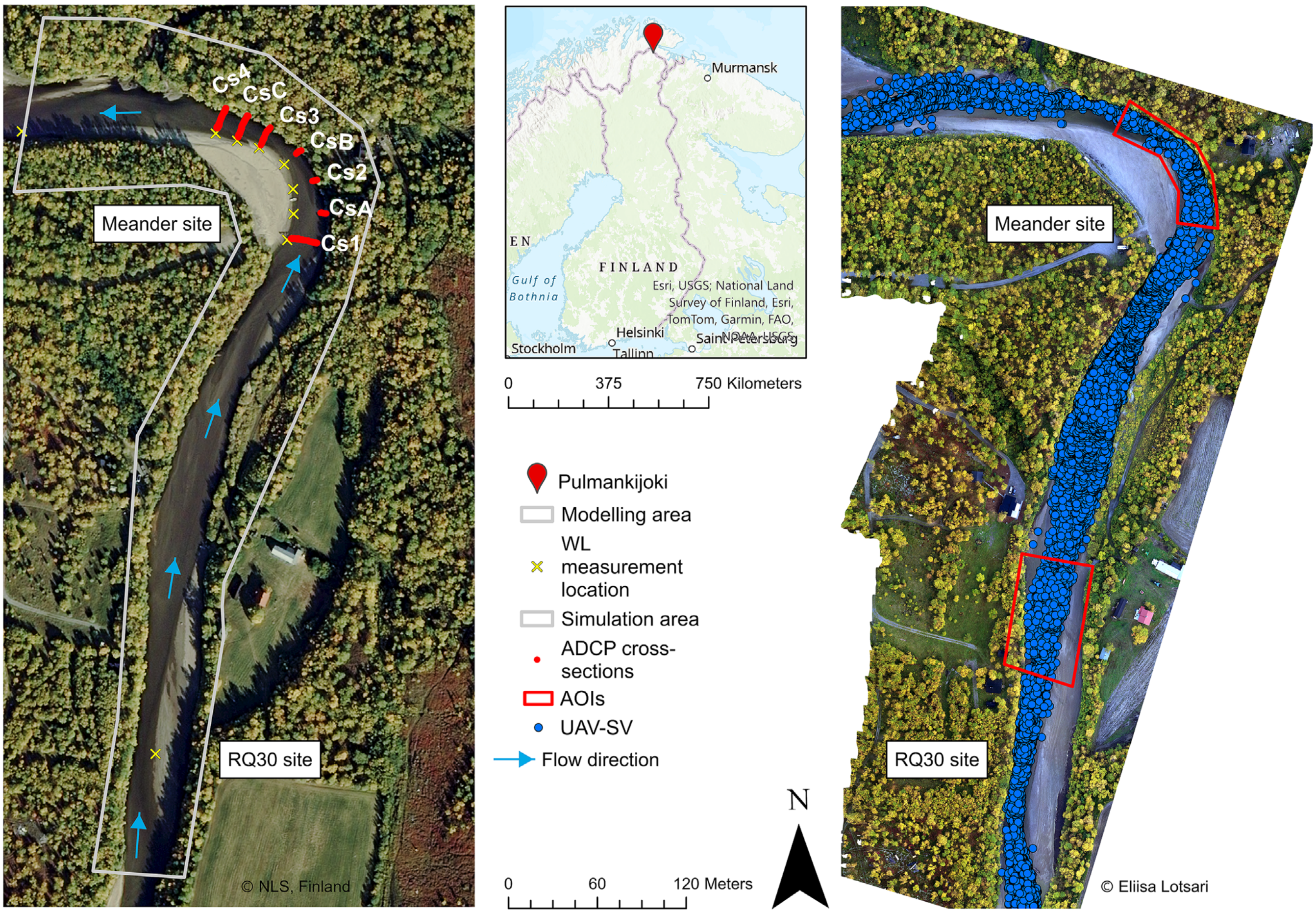

FIGURE 1 Study site of Pulmanki River in northern Finland, the arrow indicates the flow direction. The left image shows the modelling area boundary with water level measurement locations and the cross-sections for ADCP measurements. The right image shows the UAV-orthomosaic and the UAV-surface flow velocity points with selected area of interest in a meander and straight river segment. [Color figure can be viewed at wileyonlinelibrary.com]

3 | METHODS

The 2D hydrodynamic model made with Delft3D (Version 4.04.01; Deltares, 2019) comprised building and calibrating the model (Wright et al., 2017) followed by a validation process. The model includes a grid-form geometry that covers the simulation area onto which topography information is interpolated, specification of a flow resistance parameter (Manning's n) for channel and land area, and specification of boundary conditions (Figure 2). We used the discharge Q as the upstream boundary condition and the water level (WL) as the downstream boundary condition. The background horizontal viscosity was set to a uniform horizontal eddy viscosity of 0.01 ms^{-2}.

The output was a 2D hydrodynamic model simulating WL and depth-averaged velocity of a six-day period. Calibration involved adjusting Manning's n roughness values in a range of 0.023–0.035. In addition, two grid resolutions were tested (coarse: 0.7–11.4 m, fine: 0.2–4.5 m). These calibration runs were done to ensure the optimal alignment between simulated and measured water level (WL) and depth-averaged velocity (DAV). These two parameters were measured in the field at the cross-sections throughout the meander bend, and at additional WL measurement locations throughout the simulation area and period. For the UAV surface velocities, the conversion from depth-averaged velocities (DAV) to surface velocities (SV) involved applying a linear transformation using specific coefficients. This process was similarly applied to the model's DAV to obtain SV, allowing for a thorough validation from two perspectives.

3.1 | ADCP measurements and hydrographs

The measurements were conducted under shallow water depth conditions during the lowest autumn flow with the deepest water table depth recorded at approximately 1.4 m. A floating platform ("HydroBoard" by Sontek) equipped with Sontek RiverSurveyor M9 ADCP sensor was used to gather the reference data for flow velocity and water depth from the Pulmanki river reach. During the measurements, the Trimble RTK-GNSS R10 receiver (Real-Time Kinematic Global Navigation Satellite System) was applied on the ADCP platform, for gaining comparison data for the locational accuracy of the ADCP's internal DGPS (Differential Global Positioning System) sensor. The RTK-GNSS device offers accuracy within a few centimetres, whereas the internal DGPS of the ADCP provides an accuracy of approximately 50 cm. The sensor's accuracies are up to ± 0.25% of the measured velocity (SonTek, 2013). The ADCP platform was attached to the rope reaching across the river, and the measurements were coordinated by two people pulling the ADCP from one river side to the other (cf. Figure 1 for cross-section locations). Here, the sensor was always located at the upstream side of the operators to avoid

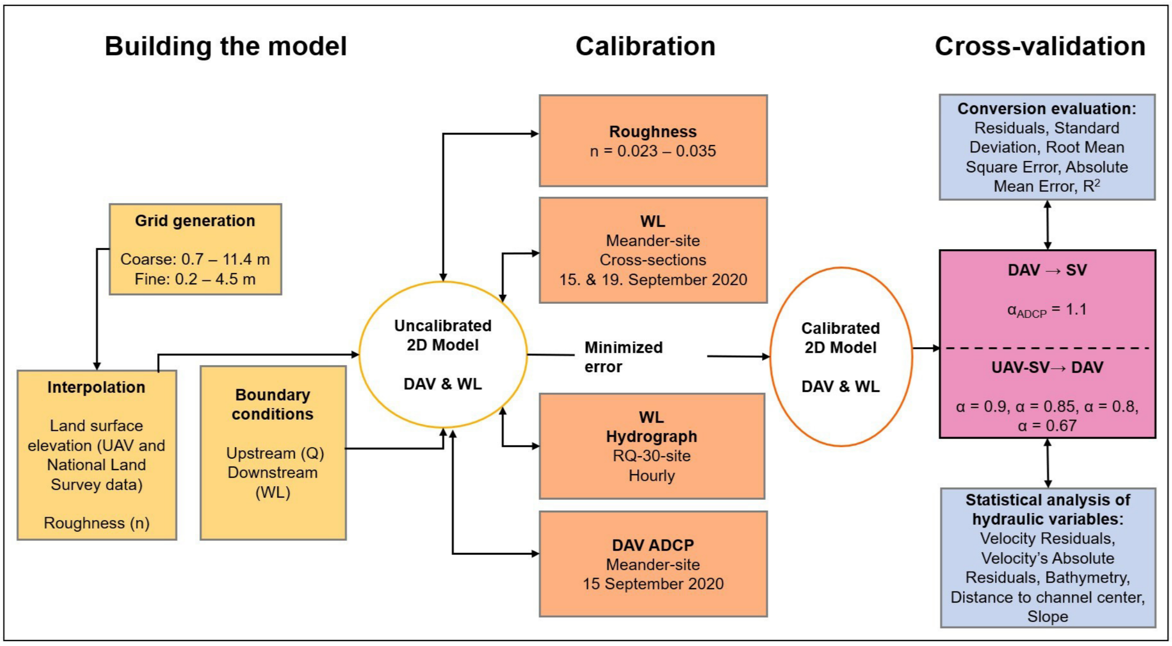

FIGURE 2 Simplified workflow of our 2D hydrodynamic modelling process, including the key variables water level (WL), depth-averaged velocity (DAV) and surface velocity (SV). It describes the basic steps of the model set-up, calibration, and cross-validation. [Color figure can be viewed at wileyonlinelibrary.com]

undesired impact during the pulling across the river. While attached to the platform, the transducer depth was 0.06 m below the water surface. Because of blanking distance the ADCP system measured the top-most cell of the water column at an average depth of 12.9 cm below the water surface. The M9 sensor was operated with 1 Hz sampling frequency. For the velocity measurements, this sensor has four 3 MHz beams and four 1 MHz beams. For the point echo sounding, it uses a 0.5 MHz vertical beam, respectively. The M9 sensor measures temporally once every second, thus the slower the cross-section is measured, the denser the measurements within cross-section. On average, the sampling distance between the points was 20 cm.

Eight cross-sections were measured on 15 September 2020 (Figure 1); one of these located at the inlet of the meander band, six within the meander band, and one downstream. The cross-sections were orientated perpendicular to the centre lines of the channel and their location measured with RTK-GNSS on the inner bank side. The measurements of the inlet area cross-section were used for defining the discharge, given the perpendicular flow from the straight reach. During the operation of the ADCP four repetitive measurements were made at each cross-section to ensure a higher accuracy in time-averaging of the acoustic ensembles. A maximum difference of 5% between the discharge values of each individual measurement was set. In addition to discharges, the sensor measures the 3D flow field and depth values of each measurement vertically. The ADCP measures velocity in water columns, which are divided into depth cells. It averages the velocity (mean values) within each depth cell based on the velocities in three different (i.e., x, y, and z) directions. It calculates the total velocity, here referred to as depth-averaged velocity (DAV), for the whole water column of each measurement vertically. Because of the 2D modelling approach in this paper this information was extracted from the raw data of each measurement location. Further, the velocity of the upper most water column, which is the closest to the surface velocity, was extracted. At 13 cm below the water surface, it does not, however, represent the actual surface velocity.

This cannot be measured directly because of disturbances arising from the device's presence and submerged transducer (Mueller et al., 2013). While this introduces uncertainties in extrapolating the water column, the use of the water column cells, including the uppermost one, is suggested as one method to obtain velocity ratios (Biggs et al., 2021). It is important to note here the potential impact of secondary currents and the velocity-dip phenomenon. According to some studies, this complex and still unsolved relationship depends on the channel structure and leads to the highest flow velocity just below the free surface, not at the water surface itself, making it different from the surface velocity (Mirauda et al., 2018, Termini & Moramarco, 2018). To process depth and velocity data in a Geographic information system (GIS) and hydrodynamic model software, the raw data was converted into ASCII files. During the post-processing, the areas with noticeable noise or interferences were deleted, also those, where the water depth was seemingly too shallow for the ADCP (<20 cm). However, we are aware that strong shears may occur affecting the velocity distribution.

For 2D unsteady modelling, boundary conditions need to be specified as a time series. WL measurements were used as the downstream boundary condition and Q as the upstream boundary condition (cf. Sect. 3.5). We recorded the Q on 15 and 18 September 2020 with the ADCP. A Solinst Levelogger 5 (Model 3,001) and Barologger 5 (Model 3,001) were installed at the RQ30-site (upstream boundary). These provided continuous water pressure data every 15 min, and after barometric compensation with recorded air pressure, continuous water depth values were gained in form of a time series covering the entire simulation period. As we measured the WL with RTK-GNSSevery 15 min at both the upstream (same location as Levelogger pressure sensor) and the downstream boundary at the water-land interface on 16 and 19 September 2020, we used the known upstream water levels to convert the continuous depth readings to continuous water level. Then the difference between upstream and downstream WL measurement locations was calculated and based on this difference between the measurement locations, the downstream WL was possible to define and thus, used as downstream boundary condition. The elevation difference was subtracted from the continuous upstream WL readings, to gain continuous WL data and also as a help for defining the Q hydrograph. The change in water level between the 15-minute time steps in the time series was calculated in percentage, and the corresponding percentage value was used to also get a time series for Q at the upstream boundary, i.e., the Q between the actual ADCP measurements were gained with this percentage method. However, the measurements of Q in the field have shown that there is no remarkable difference during that time frame (Q on 15 September was 2.19 $m3^{s-1}$; Q on 18 September was 3.24 $m3^{s-1}$). Thus, the discharges calculated between the 15 and 18 September with this percentage method are within these measured values.

3.2 | UAV-based topography and bathymetry

The land surface elevation from areas without vegetation and bathymetry were measured with remote sensing approaches. Data acquisition was done using the UAV model DJI Matrice M200 (Zenmuse X4S) at 90 m flight altitude resulting in a ground sampling distance of 2.5 cm. We distributed 11 ground control points (GCPs) evenly along the river and measured their location using RTK-GNSS with an accuracy of ±2 cm for georeferencing. The MVS-SfM photogrammetry (Eltner & Sofia, 2020; Westoby et al., 2012) was applied for calculating the surface topography. The bathymetry was derived as described in Eltner et al. (2021) using a method introduced by Dietrich (2017). Thereby, multi-media effects are considered during the 3D reconstruction and thus influences of refraction of the rays of light are roughly corrected to calculate 3D points under the water from overlapping images (for more detail see Eltner et al., 2021). The elevation data used in this study has a ground sampling distance of approx. 2 cm and was used as point data because of model input requirement in Delft3D software. However, one deeper (and darker) outer bank part of the river channel resulted in unusually low elevations. Thus, this part was also compared with ADCP's point echo sounder data, which showed that the difference between this data and the UAV-derived bathymetry data was approximately 40 cm. We therefore corrected the bathymetry based on the echo sounding data, as the UAV-bathymetry becomes more uncertain with increasing water depth (Woodget et al., 2019). The area having false values from the UAV-bathymetry was first cut out of the data, and the point echo-sounder data was combined with the UAV-bathymetry point cloud and interpolated to cover the excluded deeper area as a hybrid dataset of approx. 5 m^2. The processing of the SfM data of the land surface provided "vegetation filtered" (i.e., bare ground) elevation data. Because of the size of our simulation area, this UAV-derived elevation data did not cover the entire overbank areas. Therefore, topography data from National Land Survey Finland (NLSF) with a spatial resolution of 2 m (bare ground) was additionally included in the topographical representation of the simulation area.

3.3 | UAV-flow velocity analyses

After the bathymetry and land surface elevations had been created, the surface velocity of the entire reach could be calculated, as the approach requires the bathymetry models to mask the water areas (Eltner et al., 2021). The velocities themselves are estimated using the PTV technique, for which videos were captured flying along the river with DJI Matrice M200 (Zenmuse X4S) at 50 m altitude with a video frame rate (Hz) of 50. The head frames of the video frames were extracted after a specified interval, which depends on the flight speed and frame rate (e.g., every 100th frame). To that head frame, a defined number of tailing frames are co-registered to account for the UAV movements, eventually stabilizing a sequence of frames as if they were captured from the same perspective (Kröhnert & Meichsner, 2017). The PTV method encompasses a detection step and a tracking step. During the former step features are detected automatically based on regions of interest in the image, i.e., areas of high contrast revealing grey value gradients in at least two directions to identify distinct and unambiguous features. During the second step the features are tracked through the co-registered frames. Thereby, for regions of highest similarity are searched for, e.g., by minimizing grey value differences between the search and target image (Lucas & Kanade, 1981). The final feature tracks were then filtered considering typical flow characteristics to remove outliers (Eltner, Sardemann, & Grundmann, 2020). Eventually, the tracks were scaled by intersecting the image measurement with the water surface, which is possible because the head frame position and orientation is known from the photogrammetric bundle block adjustment, which was already used to retrieve the 3D models during the SfM processing step. For details on the specific workflow, please refer to the methodology outlined in the study by Eltner et al., 2021.

3.4 | Building the 2D hydrodynamic model

We used the Delft3D software (2D module) for the 2D hydrodynamic modelling, where the flow and dynamics are primarily influenced by horizontal variations rather than vertical ones. It solves the shallow water equations in two horizontal dimensions. Here, the grid determines the spatial resolution of the model's bathymetry, but also the spatial discretization of the conservation of mass and momentum equations of the flow during the model simulation. The grid is generated for the extent on a predefined area of interest, i.e., the simulation area. As the flood extension and height are unknown, this area is bigger than the actual channel. For each grid cell, the model computes hydrodynamic properties such as depth-averaged velocity, using a variety of equations. Here, the Navier–Stokes equations describe motion of fluid substances (e.g., viscosity) and pressure gradients. In 2D models, the quadric friction law is utilized to express the shear stress at the riverbed $(\overrightarrow{Tb})$ caused by turbulent movements within the depth-averaged flow, calculated with the following Equation (1):

$$\overrightarrow{Tb} = \frac{\rho 0 g \vec{U} \left|\vec{U}\right|}{C_{2D}^2} \tag{1}$$

where $\left|\vec{U}\right|$ is the magnitude of the depth-averaged horizontal velocity, $\rho 0$ the reference density of water, g the gravitational acceleration, and C the Chézy coefficient. The relationship between the Chézy's C and Manning's roughness coefficient (n) can be expressed as follows:

$$C = H^{1/6}/n, \tag{2}$$

where H in Equation 2 is the depth.

The grid represents the flow conditions of the river. For our model, we chose a curvilinear, boundary fitted grid to minimize errors along the boundaries and to model the flow of the river as accurately as possible (Bomers et al., 2019; Deltares, 2021; Morianou et al., 2016). The grid resolution is defined by the distribution of inserted splines across the land boundary. Splines were added in the direction upstream to downstream and cross-sectionally from left to right bank in a spatially rather equal interval to facilitate grid creation in the later steps. In locations of meander bends and possibly steeper slopes, splines were distributed more frequently and closely. Finally, the splines were converted into a grid, which was refined in areas where denser grid cells were appropriate (e.g., meander bends). Generally, the cell sizes were selected so that no morphological characteristics were lost during the refinement. For examining the impact of the grid's resolution on the model performance two grids with varying resolutions were generated that are referred to in the following as coarse (range 0.7 m–11.4 m) and fine grid (range 0.2 m–4.5 m), respectively. Note that the cells with the lowest resolution occurred at the border of the simulation area at over-bank land surface, where the water is very unlikely to occur. As a last step, the finalized grids were orthogonalized. This means that the grid shape is preserved but single points might be aligned to enhance orthogonality.

The model is computed based on interpolated bathymetry and topography point data that is fitted to the grid. For that, the UAV-derived point data set was used for the bathymetry and unvegetated land surface areas. Vegetated over-bank land surface was complemented by elevation data of NLSF to cover the entire area of interest. To keep the data quality, i.e., spatial resolution, interpolation started with the highest spatial resolution data set concluding with the lowest spatial resolution. The selected interpolation methods comprised grid cell averaging and triangular interpolation, as well as internal diffusion for grid cells that were located along the grid edges. The outcome was continuous elevation information as depth data interpolated on both grids.

3.5 | Model calibration and performance assessment

The time frame of the hydrodynamic model was set from 15 September 2020 00:00:00 until 20 September 2020 00:00:00. This period embraces the dates of the water level and velocity measurements and the UAV-flight. Despite the hydrograph being available in 15-minute steps, we converted these into 60-minute interval for the hydrodynamic modelling. This setting also ensured an acceptable computation time level, as the calibration was done several times for two grids. It ensured a comparison between the modelled results and the outcome of the field measurement. The computation time varied between the grids. The initial downstream water level for the simulation was 13.926 m. As boundary conditions, the upstream boundary was represented by Q and the downstream boundary by WL. As we applied an unsteady modelling, the values for the boundary conditions varied for each simulation day; an overview can be found in the supplement (Table S 1). This table shows the value of discharge and water level at the start of each day. An important input parameter in calibration of the hydrodynamic modelling is the choice of the roughness values (n), which depends on the grain size of the river channel and adjacent land surface. Based on literature recommendations of rivers with similar bed material (Arcement & Schneider, 1989) and case studies of the same area (Kasvi et al., 2015; Lotsari et al., 2018), a n-range between 0.025–0.04 for the river channel and 0.056 for the land surface were aimed at in the calibration process. Of these, eventually three values were chosen to represent the river channel ($n = 0.026$, $n = 0.028$, $n = 0.030$). Increasing the channel roughness value means an increase of water level at the expense of a decreased flow velocity. Therefore, the roughness adjustment is restricted by the trade-off between WL and flow velocity. We used different water level and ADCP velocity data sets for the calibration of our model resulting in three different calibration runs. First, we used the measured WL at the cross-sections on the 15 September and on the 19 September 2020 to calibrate the model. In the second run, we compared the WL of the hydrograph with the hourly output of the model at the measurement location RQ30-site. Lastly, we compared the measured depth-averaged velocity of the ADCP with those of the model.

For the calibration of the model, we assessed the model performance based on coarse and fine grid by comparing the measured water level (WL_{OBS}) at each cross-section for the 15 September 2020 and 19 September 2020 with the modelled water level (WL_{SIM}) for all three roughness values. The average of all measured and modelled cross-section WL is presented in Section 4.1. The hourly hydrograph-measurement of the WL as the second calibration run was equally assessed using the average value of the modelled WL inside the grid cell closest to the field measurement point.

The best model is used for the model validation and velocity distribution described in Section 3.6.

Model velocity performance was evaluated with average residuals as mean error (e), standard deviation of the predicted values (SD), Mean Absolute Error (MAE) and Root Mean Square Error (RMSE), and R^2. In addition, we compared the measured depth-averaged velocity (DAV_{OBS}) of the ADCP with the simulated depth-averaged velocity (DAV_{SIM}) using the same metrics. In accordance with the WL performance assessment, we stated here the performance evaluation for the average of all measured and modelled cross-section DAVs. The average of the individual, cross-sectional DAV comparison can be found in the supplement.

3.6 | Cross-validation and conversion performance

Our cross-validation approach consists of two velocity conversions using fixed coefficients to convert depth-averaged velocity to surface velocity and vice versa to evaluate conversion performance. In this process, we used different data sets and further examined how key hydraulic variables (depth, water surface elevation, and channel width) influence the flow dynamics and velocity patterns in the river and how these may contribute to the uncertainty arising from velocity conversion. The conversions may vary with the hydraulic radius and the underlying physical variables (Johnson & Cowen, 2017). However, we hypothesize that the site-conditions of our study site (i.e., natural, shallow, transparent, non-vegetated) may allow the application of a fixed coefficient and we examine this accordingly. For the validation and performance assessment we only considered the coarse grid and the result of $n = 0.026$. Moreover, we did the validation and velocity analysis for the entire reach and for two areas of interest (AOIs) representing a meander and a straight river segment.

We calculated the ratio of the ADCP's recorded depth-averaged velocity (DAV_{OBS}) and near surface velocity (SV_{OBS}) of each cross-section measurement location using a simple linear regression. The result was a velocity coefficient for each measurement point. To assess the simplicity of the regression and potential influence of hydraulic variables, a centreline was drawn through the channel, and the distances from the measurement points to this line were calculated using the ESRI ArcGIS Pro (version 3.1.2) Near tool (planar distance in meters) to acknowledge channel widths. This and three key hydraulic variables recorded with the ADCP comprising depth, water surface elevation and bathymetry were used to analyse their relationship with the velocity coefficients.

Afterwards, we calculated the average of these coefficients and obtained a fixed one referred to as $\alpha_{ADCP} = 1.11$. With this, we first calculated the continuous modelled depth-averaged velocity (DAV_{SIM}) into surface velocity (SV_{CAL}) receiving a continuous surface velocity grid. This was subsequently compared with our reference data, the UAV-surface velocity points (SV_{UAV}) by considering only velocities over 0.1 m^{s-1} due to the accuracy decrease at lower velocities. We took those points that matched a cell of the model grid and compared it with the cell's simulated DAV value; if several points matched one cell, we used the average value. Eventually, the average of all SV_{UAV} and corresponding SV_{CAL} values were considered for the cross-validation and conversion performance assessment for the entire study reach and separately for the AOIs. Secondly, we calculated the UAV-surface velocities to DAV. Genç et al. (2015) and Hauet et al. (2018) describe in their study several fixed coefficients ($\alpha = 0.9$, 0.85, 0.80, and 0.67) that we test in our application as experimental values. This enabled the conversion of our discontinuous (point) UAV-SV data into discontinuous DAV data (DAV_{CAL}) and compared DAV_{CAL} with our reference data, the numerical model predictions (DAV_{SIM}).

Lastly, we analysed if uncertainties arising from fixed coefficients can be explained by key hydraulic variables affecting the flow distribution in the river. For this, we tested the conversion performance by including available information of the hydraulic radius as derived by UAV-data. Here, in addition to bathymetry, we used also the distance to the channel centre calculated in ArcGIS Pro (Near tool, planar distance in meters) and derived the slope information of each pixel from the bathymetry data with the tool Slope (unit in degree).

3.7 | Statistical and multivariate analysis

We applied exploratory data analysis and multivariate statistical analysis to evaluate the relationship between the coefficients derived by the linear regression of the ADCP velocities and the selected hydraulic variables measured with this device. We used in the following Spearman's rank correlation as a non-parametric test and a linear regression model. It was further tested if the coefficients exhibited distinct spatial patterns using Moran's I spatial autocorrelation test with a distance threshold of 30 cm.

The cross-validation and performance assessment of the velocity conversion in both directions involved the statistical metrics described in Section 3.6 and key hydraulic variables for Spearman's rank correlation. Statistical analysis was performed with R statistical computing environment version 4.2.3 (R Core Team, 2022) choosing a significance level (p-value) of < 0.05.

4 | RESULTS

The results are divided into three sections. The first covers the model calibration and model performance. The last two sections elaborate on the findings of the cross-validation and velocity conversion performance.

4.1 | Calibration enhancement

For the first calibration run we used the average of the WL_{OBS} measured at the cross-sections on the 15 September and on the 19 September 2020 and compared this with WL_{SIM} of the closest grid cell. The calibration results with of all roughness values show very good results for the 15 September 2020. The maximum bias in WL_{OBS} and WL_{SIM} was approximately ± 1 cm for both grids. Both MAE and RMSE indicate here a small average magnitude of errors (0.017–0.019 m s^{-1}) and a rather high precision with standard deviations ranging between 0.041–0.048 m s^{-1}. While the accuracy decreased and the bias increased for the 19 September 2020, the difference remained within ± 10 cm for both grids (cf. Table 1) with similar precision. The WL predicted on the fine grid tended to perform slightly better than the one modelled on the coarse grid. Among the roughness values, $n = 0.026$ reaches the best results.

Then, we compared the WL of the hydrograph with the hourly output of the model at the measurement location RQ30-site. The output WL from the respective grid cell that covered the measurement point location was taken. However, the model grid representing the WL as continuous data reaches the measurement point at different time steps depending on the roughness value. Therefore, there are three different measured water levels taken from the hydrograph with corresponding simulation value. Table 2 shows the average WL of the entire hydrograph WL_{OBS} compared with the average simulated, hourly output WL_{SIM}, with the difference being <16 cm. It appears that the fine grid provided a marginally improved representation of the observed data compared with the coarse grid but no overall substantial difference between the grids (cf. Table 1). In accordance with the previous calibration set of the WL from 15 and 19 September 2020, the roughness value of 0.026 produces the best results for both grids with a difference of −14.4 cm and −14 cm, respectively (cf. Table 2). Yet, this calibration run clearly exhibits the least agreement between observed and predicted variables (cf. Table 2).

Lastly, our third set of calibration runs aimed to compare DAV_{OBS} of the ADCP measurement and DAV_{SIM} of the model. Table 3 shows the average values of the DAV_{OBS} point data for all cross-sections (outliers removed) for which the corresponding DAV_{SIM} was extracted at the respective grid location. The findings point out a moderate precision of the model, however, with a low bias and with about 78–82% of the variance in the observed velocities explained by the models (cf. Table 3). The model based on $n = 0.026$ performed the best with a velocity difference of 0.052 m s^{-1} and a MAE of 0.08 m s^{-1} for the

TABLE 1 First calibration set comparing the average water level measured at the cross-sections (WL_{OBS}) with the modelled water levels (WL_{SIM}) for all roughness values and grids using standard deviation (SD), residuals (e), and R^2 (if applicable, unit in m).

	Coarse grid			Fine grid		
15 September 2020	**n = 0.026**	**n = 0.028**	**n = 0.03**	**n = 0.026**	**n = 0.028**	**n = 0.03**
WL_{OBS} (m)	14.004	14.004	14.004	14.004	14.004	14.004
WL_{SIM} (m)	14.002	14.008	14.014	13.992	13.997	14.001
SD	0.044	0.046	0.048	0.041	0.042	0.042
e	0.002	−0.004	−0.01	0.012	0.007	0.003
RMSE	0.020	0.021	0.019	0.021	0.020	0.019
MAE	0.018	0.019	0.019	0.019	0.019	0.017
R^2	0.768	0.762	0.753	0.771	0.755	0.763
	Coarse grid			**Fine grid**		
19 September 2020	**n = 0.026**	**n = 0.028**	**n = 0.03**	**n = 0.026**	**n = 0.028**	**n = 0.03**
WL_{OBS} (m)	14.010	14.010	14.010	14.010	14.010	14.010
WL_{SIM} (m)	14.112	14.103	14.112	14.077	14.084	14.093
SD	0.045	0.048	0.048	0.052	0.052	0.053
e	−0.102	−0.093	−0.078	−0.067	−0.074	−0.083
RMSE	0.081	0.096	0.105	0.070	0.077	0.085
MAE	0.080	0.093	0.102	0.067	0.074	0.083
R^2	0.771	0.781	0.784	0.7894	0.792	0.774

TABLE 2 Second calibration set comparing the average water level measured (WL_{OBS}) at the RQ-30 site and the average modelled water level (WL_{SIM})for all roughness values and grids using standard deviation (SD), the residuals (e), and R^2 (if applicable, unit in m).

	Coarse grid			Fine grid		
Hourly output	**n = 0.026**	**n = 0.028**	**n = 0.03**	**n = 0.026**	**n = 0.028**	**n = 0.03**
WL_{OBS} (m)	14.285	14.272	14.272	14.288	14.287	14.272
WL_{SIM} (m)	14.429	14.419	14.432	14.428	14.440	14.425
SD	0.030	0.042	0.044	0.028	0.030	0.046
e	−0.144	−0.147	−0.16	−0.14	−0.153	−0.153
RMSE	0.145	0.148	0.160	0.141	0.154	0.155
MAE	0.147	0.147	0.160	0.141	0.154	0.153
R^2	0.996	0.996	0.997	0.997	0.997	0.995

TABLE 3 DAV calibration metrics showing the average velocity value of all cross-sections (DAV_{OBS}) compared to the average, modelled velocity (DAV_{SIM}) for all roughness values and grids using standard deviation (SD), the residuals (e), root mean square error (RMSE), mean absolute error (MAE), and R^2 (if applicable, unit in m s^{-1}).

	Coarse grid			Fine grid		
15 September 2020	**n = 0.026**	**n = 0.028**	**n = 0.03**	**n = 0.026**	**n = 0.028**	**n = 0.03**
DAV_{OBS}	0.385	0.385	0.385	0.382	0.382	0.382
DAV_{SIM}	0.333	0.325	0.323	0.307	0.304	0.299
SD	0.191	0.176	0.170	0.189	0.179	0.171
e	0.052	0.06	0.062	0.075	0.078	0.083
RMSE	0.104	0.107	0.107	0.112	0.113	0.117
MAE	0.080	0.084	0.084	0.088	0.089	0.093
R^2	0.785	0.782	0.786	0.820	0.827	0.823

coarse grid resolution and 0.075 m s^{-1} a and a MAE of 0.088 m s^{-1} for the fine grid resolution. The results thus hint towards a slightly more accurate agreement reached by the coarse grid resolution (cf. Table 3).

4.2 | Depth-averaged velocity conversion

At first, we examined if the velocity coefficients calculated at each ADCP measurement location vary in relation to key variables

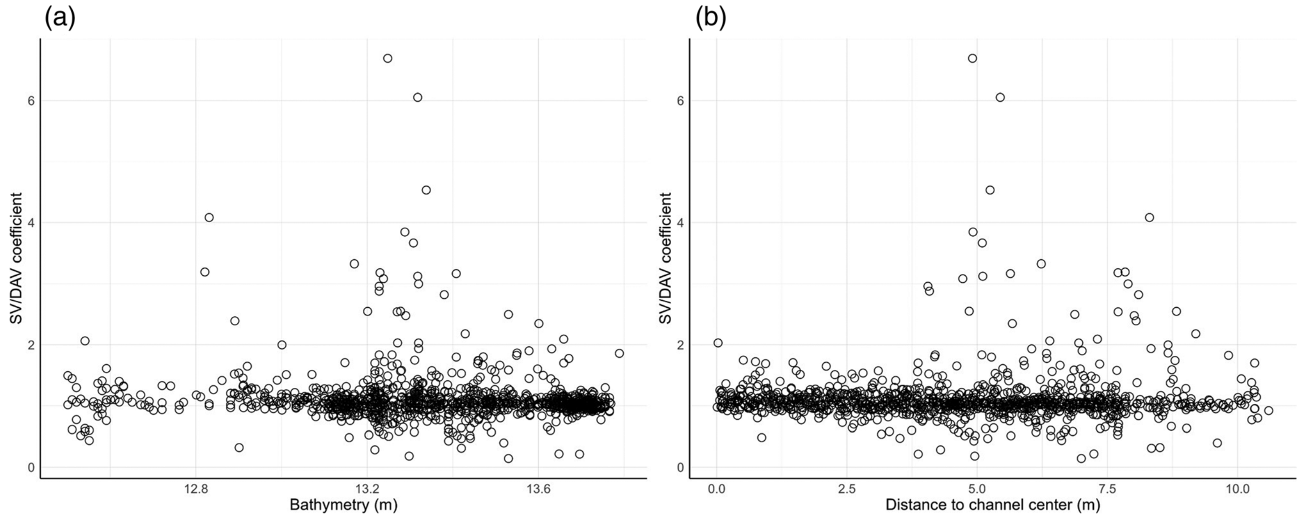

FIGURE 3 Distribution of the coefficients obtained from simple linear regression using depth-averaged velocity and near-surface velocity data from the ADCP device plotted against bathymetry (left panel, a) and distance to the channel centre (right panel, b).

TABLE 4 Comparison of UAV surface velocities (SV_{UAV}) and with $\alpha_{ADCP} = 1.11$ calculated surface velocities (SV_{CAL}) for the entire study reach and AOIs with n = 0.026 using standard deviation (SD), the residuals (e), root mean square error (RMSE), mean absolute error (MAE), and R^2 (if applicable, unit in m s^{-1}).

	Entire reach	Straight AOI	Meander AOI
SV_{UAV}	0.572	0.547	0.561
SV_{CAL}	0.526	0.480	0.662
SD	0.135	0.065	0.150
e	0.046	0.067	−0.101
RMSE	0.125	0.092	0.180
MAE	0.097	0.079	0.146
R^2	0.347	0.601	0.223

(i.e., depth, water surface elevation, bathymetry, and distance to channel centre). There was no statistically significant relationship between the coefficients and any of the variables, underlined also in the data distribution (cf. Figure 3). In addition to this finding, the Moran I test did not give any evidence for spatial autocorrelation.

Using afterwards the average value of the coefficients $\alpha_{ADCP} = 1.11$ to convert our continuous model DAV into surface velocity (SV_{CAL}) generally suggested moderate conversion performance when comparing it with the SV_{UAV} point data for the entire reach with significant differences between the AOIs (cf. Table 4). There is room for improvement, specifically in reducing the overestimation of the velocities. The analysis for the entire reach indicated a positive relationship with moderate strength for velocity residuals and bathymetry. This means, as bathymetry increases (or in shallower areas), the model tends to overestimate the velocities. This is the most pronounced in the rather straight river segment along the main flow (cf. Figure 4). Testing the velocity performance (absolute residuals) showed, however, only very weak to negligible relationships regarding bathymetry, slope, and distance to channel centre. This implies that there is no explainable variation in performance based on these factors.

The straight AOI exhibited a higher MAE and RSME (0.079 m s^{-1}, 0.092 m s^{-1}, respectively) than the meander AOI (0.146 m s^{-1} and 0.180 m s^{-1}, respectively). Consequently, the conversions yielded higher accuracy for the SV_{UAV} in the straight river reach, while showing poorer agreement in the meander. Further, the model overestimates the velocities in the meander bend with e = −0.101 m s^{-1}; this great bias is highlighted in Figure 3. The analysis suggested bathymetry as a variable with negative, significant, yet weak impact on both, velocity residuals and the absolute residuals for the straight AOI. This points to an underestimation, yet more accurate velocity conversion in shallow areas (contrary to the correlation result for the entire reach).

4.3 | UAV-surface velocity conversion

The second direction of velocity conversion was from UAV-surface velocity into depth-averaged velocities (DAV_{CAL}) with four suggested fixed coefficients (i.e., α = 0.67, α = 0.8, α = 0.85, α = 0.9). We subsequently compared these with our original depth-averaged velocity model output (DAV_{SIM}). This velocity conversion generally resulted in a moderate performance for the entire simulation area. The conversion with the coefficient α = 0.67 yielded the least accurate outcome, in terms of a higher RMSE (0.137 m s^{-1}) and MAE (0.102 m s^{-1}). Contrary, the coefficients α = 0.8 and α = 0.85 had a slightly lower RSME of 0.110 m s^{-1} and 0.111 m s^{-1}, respectively, and an MAE of 0.077 m s^{-1} and 0.080 m s^{-1} (cf. Table 5). The assessment showed that the variable slope did not play a significant role in relation to velocity residuals for the entire reach. However, the residuals showed a significant negative relationship with weak strength in the correlation with bathymetry, demonstrating a faint impact of water depths on model underestimation. The coefficient α = 0.67 exhibited this relationship also for the absolute residuals, thus, the velocity conversion tends to perform better in shallower waters. Otherwise, the performance of the velocity conversion indicated no other association with the hydraulic variables for the remaining coefficients.

The velocity conversion performance also varied here among the AOIs based on river morphology (Figure 5). Similarly to the opposite velocity conversion as described in Section 4.2, this velocity conversion reaches better results for the straight AOI with R^2 = 0.620

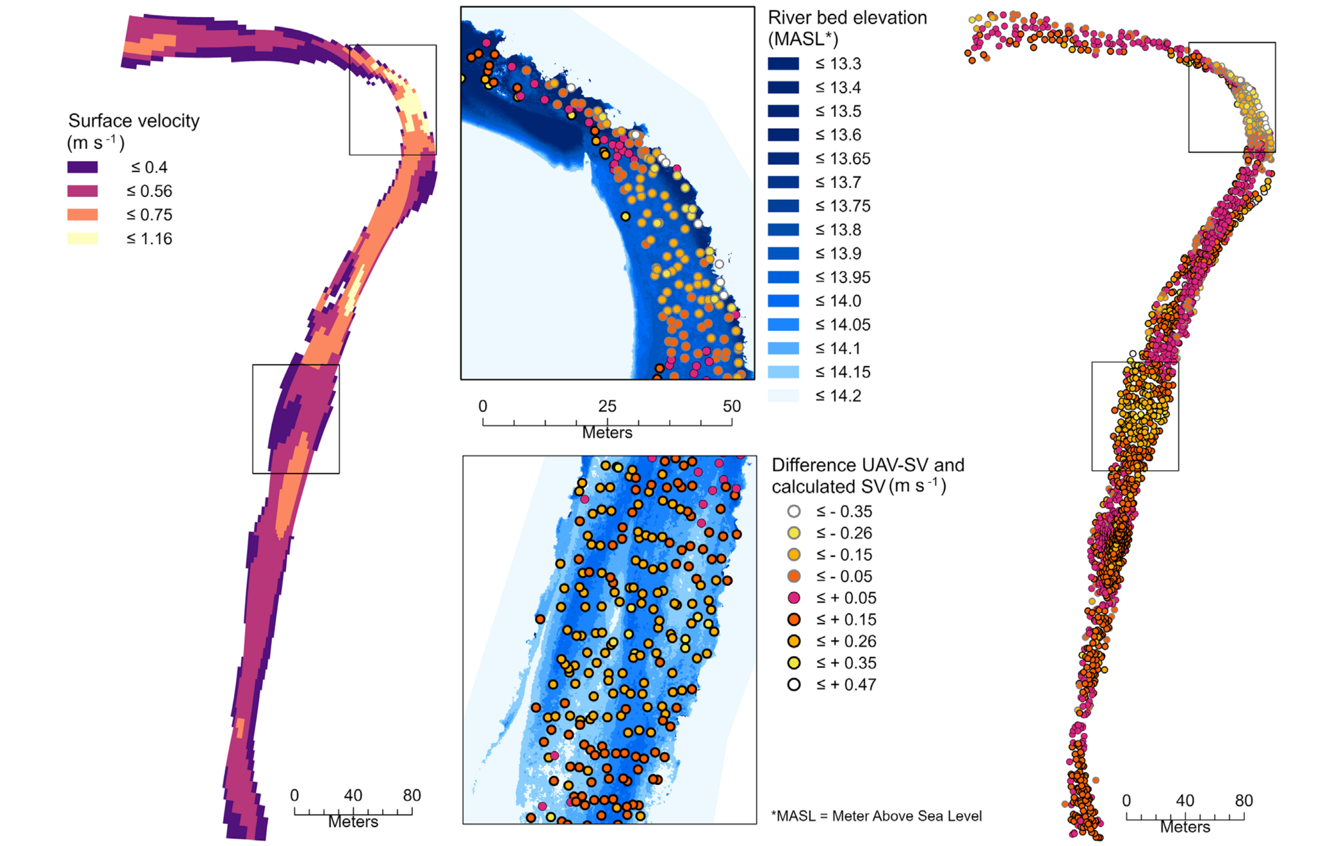

FIGURE 4 Surface velocity (SV_{CAL}) in m s^{-1} derived with $\alpha_{ADCP} = 1.11$ from the continuous model DAV (left). The difference of this and corresponding UAV-surface velocity point data (SV_{UAV}) is shown on the right for n = 0.026. Small areas show these residuals in relation to bathymetry in the middle. Black outlined points indicate model underestimation, grey outlined points overestimation. [Color figure can be viewed at wileyonlinelibrary.com]

TABLE 5 Match of modelled (DAV_{SIM}) and calculated depth-averaged velocity (DAV_{CAL}) derived from the UAV-surface velocity using selected coefficients covering the entire study reach and selected AOIs using standard deviation (SD), the residuals (e), root mean square error (RMSE), mean absolute error (MAE), and R^2 (if applicable, unit in m s^{-1}).

Entire reach	α = 0.67	α = 0.80	α = 0.85	α = 0.90
DAV_{SIM}	0.466	0.466	0.466	0.466
DAV_{CAL}	0.378	0.452	0.480	0.508
SD	0.105	0.108	0.111	0.112
e	0.088	0.014	−0.014	−0.042
RMSE	0.137	0.110	0.111	0.120
MAE	0.107	0.077	0.080	0.090
R^2	0.347	0.347	0.347	0.347

	Meander AOI							
Straight AOI	α = 0.67	α = 0.80	α = 0.85	α = 0.90	α = 0.67	α = 0.80	α = 0.85	α = 0.90
DAV_{SIM}	0.435	0.435	0.435	0.435	0.571	0.571	0.571	0.571
DAV_{CAL}	0.368	0.439	0.466	0.494	0.364	0.435	0.462	0.490
SD	0.044	0.052	0.055	0.059	0.149	0.146	0.145	0.145
e	0.067	−0.004	−0.031	−0.059	0.206	0.136	0.108	0.082
RMSE	0.08	0.052	0.063	0.083	0.254	0.199	0.181	0.166
MAE	0.07	0.042	0.053	0.070	0.225	0.168	0.148	0.132
R^2	0.620	0.620	0.620	0.620	0.406	0.406	0.406	0.406

compared with the meander AOI with an R^2 of 0.406 (Figure 6). In the straight AOI, the coefficient α = 0.8 appears to be the most effective with an RMSE of 0.052 m s^{-1} and an MAE of 0.042 m s^{-1} and a negligible bias. The conversion performance in the meandering reach is generally poor to moderate with the best results achieved with α = 0.9. In contrast, α = 0.67 was the least favourable coefficient (cf. Table 5).

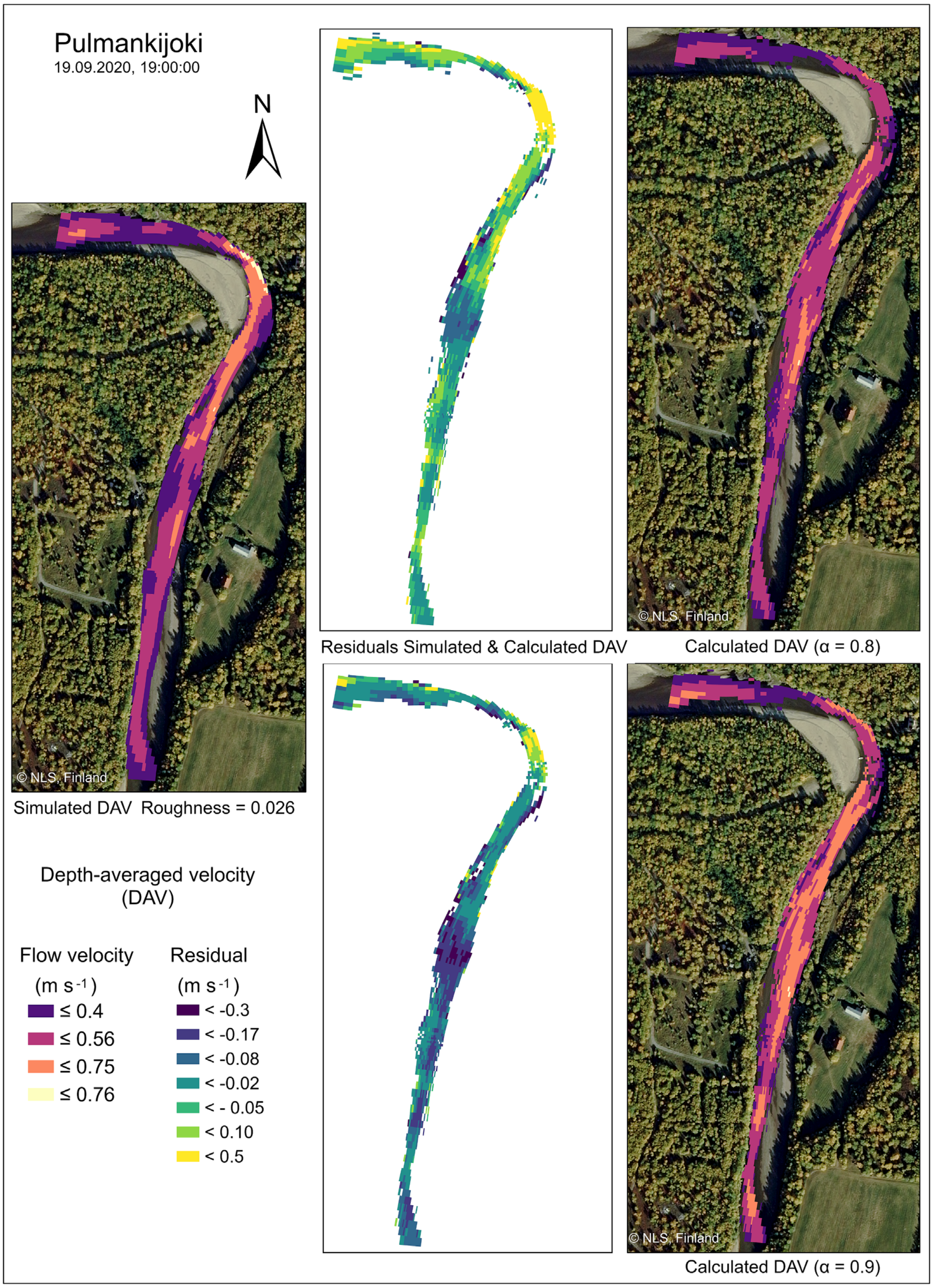

FIGURE 5 The modelled depth-averaged velocity (DAV_{SIM}) in m s^{-1} (left panel) and the calculated depth-averaged velocity (DAV_{CAL}) using $\alpha = 0.8$ upper right panel) and $\alpha = 0.9$ (lower right panel). The difference between the modelled and calculated DAVs is expressed as residuals as shown in the middle. [Color figure can be viewed at wileyonlinelibrary.com]

The residuals showed a bias ranging from 0.082 m s^{-1} to 0.206 m s^{-1} and a noteworthy decrease in accuracy with lower coefficient.

The analysis of the hydraulic variables in relation to the velocity conversion showed controversial outcomes between the AOIs. The straight reach indicated a moderate positive relationship between the residuals and bathymetry for $\alpha = 0.8$ and $\alpha = 0.85$. However, the correlation of absolute residuals and bathymetry exhibited a moderate negative relationship for $\alpha = 0.9$ and $\alpha = 0.67$. In opposite to these findings, the meander segment showed a moderate, positive relationship for the velocity residuals of all coefficients (excl. $\alpha = 0.67$) and the distance to the channel centre.

5 | DISCUSSION

Our 2D hydrodynamic model comprised of six consecutive days and three calibration runs. It was built upon two grids with varying resolution, onto which high resolution UAV-derived bathymetry data was

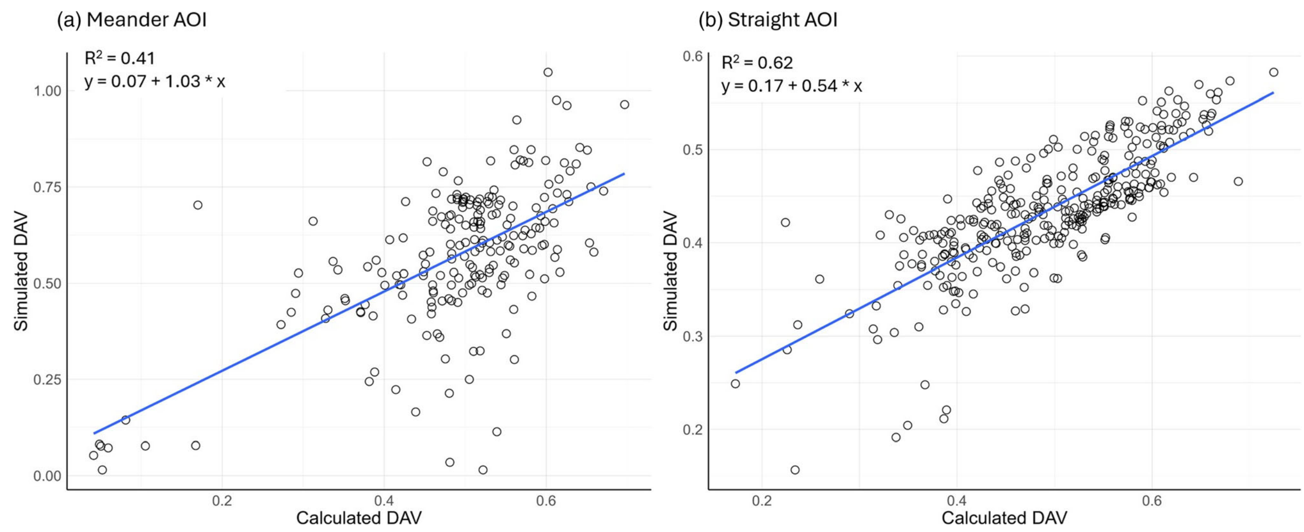

FIGURE 6 The model's simulated depth-averaged velocity (DAV_{SIM}) and the equivalent velocity calculated with $\alpha = 0.9$ (DAV_{CAL}) for the meander area of interest (a) and the straight area of interest (b) in m s^{-1}. [Color figure can be viewed at wileyonlinelibrary.com]

interpolated. Very good model performance for WL and DAV on both grids reached the n-value 0.026 like previous findings (cf. Lotsari et al., 2010; Kasvi et al., 2015). Hunter et al. (2008) tested the meaning of grids and underlying bathymetry data concluding these determine the hydrodynamic model quality substantially. Our good results might be due to the integration of high resolution UAV-bathymetry data and the curvilinear grid. We used a fixed roughness value for modelling because of the uniform sediment material in the field, but spatially varying information could enhance the model outcomes further. This is, however, difficult to implement owing to unfixed bed roughness boundaries and interaction in the system (Pappenberger et al., 2005).

Our cross-validation approach converted velocities in both directions with fixed coefficients: DAV to SV and vice versa. As we examined the possible relationships between the coefficients derived from ADCP velocities and hydraulic variables at each location prior to the model validation and performance, employing a fixed coefficient ($\alpha_{ADCP} = 1.1$) for calculating the model's DAV into SV seemed justified here. Additionally, our dataset does not exhibit spatial autocorrelation, indicating spatial uniformity and homogeneity in the meander river segment. Despite these findings it is important to note that ADCP measurements do not directly capture immediate surface velocity, and therefore, the results should be interpreted with caution. At the free surface, the velocity might be lower than right below it because of secondary flows, including secondary currents, shear stresses, and the velocity-dip (Miraud & Russo, 2019; Termini & Moramarco, 2018). Moradi et al. (2019) presented processing methods to identify secondary flows in the ADCP data. These methods could be applied to rule out initial uncertainties of velocity distribution within the water columns. Our spatial and statistical analysis highlighted a decrease in velocity conversion performance with $\alpha_{ADCP} = 1.1$ for deeper areas. Deeper areas are particularly located in the meander bend, for which the conversion performance has been poor. While one cause could be the cell location of 15 cm below the surface used to obtain the near surface velocity, another cause could have been the velocity distribution in the water column itself (e.g., less homogeneity). The usage of the water columns cells until the upper most is suggested to be nonetheless one method to obtain velocity ratios (Biggs et al., 2021).

As a difference in velocity conversion performance between the AOIs was also apparent for the conversion from surface to depth-averaged velocities, our results underscore the sensitivity to geomorphic features. The expected, more complex flow patterns in the meander (and more complex hydraulic variables) may explain the poor conversion performance and underestimation of velocities in the meander section. Although $\alpha = 0.9$ reached slightly higher results, it cannot be concluded that this coefficient performed well. This coefficient is common for artificial, concrete rivers (Hauet et al., 2018), which is clearly not the case for the meander section. The analysis suggests an impact of the distance to the channel centre on the conversion accuracy, yet bathymetry is surprisingly no significant factor here. On the other hand, the fact that the conversion accuracy was notably good in a straight and simple stretch suggests that the conversion approach is effective using $\alpha = 0.8$. Genç et al. (2015) stated that a coefficient of 0.67 and lower is applied for shallow waters. Our results cannot confirm this, because of the definition vagueness for "shallow". The obtained results align with those reported by Bandini et al. (2022).

While the cross-validation takes into consideration velocity conversions into both directions and also analysed the conversion's accuracy (i.e., over- and underestimation) regarding selected hydraulic variables, two potential uncertainty sources are evident. First, the reference source is for one conversion direction of the modelled DAV and for the other conversion the UAV surface velocities. These have an uncertainty margin that may have led to mismatches when compared with the converted velocities. Secondly, the conversions are based on fixed velocity coefficients, whose application across a spatially heterogenous area may result in a bias. In an integrated approach like ours, it is not indicated which one is the most dominant. As model calibration and validation uncertainties including the velocity conversions go hand in hand, spatially varying parameters are needed to reflect site-conditions truthfully. A spatially varying roughness parameter could enhance calibration particularly in the immediate transition of channel and land surface. In further studies, continuous data on roughness could be derived also with UAVs. Hauet et al. (2018) pointed out that the relation of velocity conversion coefficients depends among others on roughness. Variation in roughness and depths is likely to have a substantial influence on the overall model and validation performance for the simulation area length of 1 km. Despite the great potential to use UAV-information for hydrodynamic modelling, deriving UAV-bathymetry and -topography is limited to shallow and transparent waters. Deep areas and those with apparent surface turbulence should be verified with other devices, among others TLS or ADCP measurements (as also noted by Kasvi et al., 2019 and Woodget et al., 2019). Our results however show that even with fixed coefficients the modelled and converted velocities reach a good agreement for the straight river section. Further, they show regardless of the uncertainty source which locations and hydraulic variables are related to the conversion bias and accuracy. This spatial analysis enhances thus the understanding of a coupled numerical-experimental approach.

This study concentrated on video-based PTV. However, further investigations could explore additional methods such as static recording and local time-averaged ADCP measurements of 2–5 min to study potential macro-turbulences (cf. Lotsari, Dietze, et al., 2020). Understanding the occurrence and impact of such turbulences on UAV-flow velocity detection would contribute to the integration of traditional and remote sensing techniques, as well as enhance their interpretation. This study investigated the use of fixed coefficients in a numerical-experimental framework and the uncertainty of using these in a vice versa cross-validation approach. The use of devices such as surface velocity flow radars to obtain an accurate measurement of surface velocities would improve this assessment even further, although the conversion from surface to depth-averaged velocity is more common (Biggs et al., 2023). Another UAV-variable that can be included in the calibration and validation process in further studies is the WL derived by UAV-photogrammetry (Eltner et al., 2021), adding another spatially continuous variable as reference. Our study highlights segment-specific calibration or adjustment of conversion coefficients and the need for a targeted concept. Further research could apply machine learning techniques, for instance multiple linear regression using the velocity distribution and hydraulic variables recorded with the ADCP instrument, and, in turn, the UAV-information for a spatially more comprehensive approach.

6 | CONCLUSIONS

Our study used UAV-reference data to enhance 2D hydrodynamic modelling of long river segments under shallow water and open channel conditions. We successfully calibrated the models of two grid resolutions with three calibration runs using field data sets. The velocity conversions exhibited coherence, with both directions showing consistent trends, such as velocity bias with varying bathymetry. The consistent differences between the meander and straight sections in both conversion directions emphasise the segment-specific patterns. The cross-validation approach, which incorporated hydraulic variables and velocities derived from UAV data alongside fixed velocity coefficients, demonstrated the potential of using UAV data, particularly in straight river reaches. Notably, the coefficient $\alpha = 0.8$ emerged as the most suitable choice. The good agreement between converted velocity and reference data highlights the success of the integrated use of UAV-flow velocities and conversion coefficients for this section. The poor performance in the meander underscores the necessity for a more sophisticated approach to velocity conversion in regions with complex flow dynamics.

AUTHOR CONTRIBUTIONS

EL and AE planned the campaign and EL took responsibility for research planning and supervision. FW, EL, DS, ME, and AE performed the measurements. EL, AE and FW prepared the data, FW analysed the data. FW prepared the manuscript with contributions from all co-authors.

ACKNOWLEDGEMENTS

We would like to thank Marko Kärkkäinen for his data quality check and Mariana Verdonen for the field assistance. The Research Council of Finland and DAAD (Germany) supported the study financially via the mobility project "Hydro-morphological change detection of rivers in cold climate regions with integrated spatio-temporal high resolution methods" (332563). The Department of Geographical and Historical Studies, University of Eastern Finland supported the work financially. The funding for the field salaries of authors from the University of Eastern Finland and Aalto University was provided by the Academy of Finland2 (HYDRO-RDI-Network, grant number: 337394; DefrostingRivers, grant number: 338480).

CONFLICT OF INTEREST STATEMENT

The authors declare that they have no conflict of interest.

DATA AVAILABILITY STATEMENT

The bathymetry, topography, UAV flow velocity and ADCP velocity data is available upon request.

ORCID

Franziska Wolff https://orcid.org/0000-0002-6667-4169
Eliisa Lotsari https://orcid.org/0000-0002-0120-8722
Melanie Elias https://orcid.org/0000-0003-2169-8762
Anette Eltner https://orcid.org/0000-0003-2065-6245

REFERENCES

Arcement, G.J. & Schneider, V.R. (1989) Guide for selecting Manning's roughness coefficients for natural channels and Flood Plains. *United States Geological Survey Water-Supply Paper*, 2339, Washington: U.S. G.P.O. Available from: https://doi.org/10.3133/wsp2339

Bandini, F., Frias, M.C., Liu, J., Simkus, K., Karagkiolidou, S. & Bauer-Gottwein, P. (2022) Challenges with regard to unmanned aerial systems (UASs) measurements of river surface velocity using Doppler radar. *Remote Sensing*, 14(5), 1277. Available from: https://doi.org/10.3390/rs14051277

Biggs, H., Smart, G., Doyle, M., Eickelberg, N., Aberle, J., Randall, M. & Detert, M. (2023) Surface velocity to depth-averaged velocity—a review of methods to estimate alpha and remaining challenges. *Water*, 15, 3711. Available from: https://doi.org/10.3390/w15213711

Biggs, H., Smart, G., Holwerda, N., Doyle, M., McDonald, M. & Ede, M. (2021) River discharge from surface velocity measurements - A field guide for selecting alpha. Envirolink Advice Report. Christchurch, New Zealand.

Blanckaert, K. (2018) Hydro-sedimentological processes in meandering rivers. In: Ghinassi, M., Colombera, L., Mountney, N.P., Reesink, A.J.H. & Bateman, M. (Eds.) *Fluvial meanders and their sedimentary products in the rock record*. John Wiley & Sons, Ltd. Available from: https://doi.org/10.1002/9781119424437.ch12

Bomers, A., Schielen, R.M.J. & Hulscher, S.J.M.H. (2019) The influence of grid shape and grid size on hydraulic river modelling performance. *Environmental Fluid Mechanics*, 19, 1273–1294. Available from: https://doi.org/10.1007/s10652-019-09670-4

Brauneck, J., Gattung, T. & Juepner, R. (2019) Surface flow velocity measurements from UAV-based videos. *The Internaltional Archives of the Photogrammetry, Remote Sensing and Spatial Information Sciences*, XLII-2/W13, 221–226. Available from: https://doi.org/10.5194/isprs-archives-XLII-2-W13-221-2019

Dealtares. (2021) DELFT3D-flow. Simulation of multi-dimensional hydrodynamic flows and transport phenomena, including sediments, Hydro-Morphodynamics. User manual. Delft, Netherlands: Dealtares.

Deltares. (2019) Delft3D-FLOW User Manual (Version 4.04.01). Deltares.

Detert, M., Johnson, E.D. & Weitbrecht, V. (2017) Proof-of-concept for low-cost and non-contact synoptic airborne river flow measurements. *International Journal of Remote Sensing*, 38(8–10), 2780–2807. Available from: https://doi.org/10.1080/01431161.2017.1294782

Dietrich, J.T. (2017) Bathymetric structure-from-motion: extracting shallow stream bathymetry from multi-view stereo photogrammetry. *Earth Surface Processes and Landforms*, 42(2), 355–364. Available from: https://doi.org/10.1002/esp.4060

Eltner, A., & Sofia, G. (2020) Structure from motion photogrammetric technique. Tarolli, P. & Mudd, S.M. (Eds.), *Developments in Earth Surface Processes*. Elsevier, 23. Available from: https://doi.org/10.1016/B978-0-444-64177-9.00001-1

Eltner, A., Bertalan, L., Grundmann, J., Perks, M.T. & Lotsari, E. (2021) Hydro-morphological mapping of river reaches using videos captured with UAS. *Earth Surface Processes and Landforms*, 46(14), 2773–2787. Available from: https://doi.org/10.1002/esp.5205

Eltner, A., Hoffmeister, D., Kaiser, A., Karrasch, P., Klingbeil, L., Stöcker, C., & Rovere, A. (2020) *UAVs in environmental sciences – methods and applications*. Darmstadt, Germany: WBG Academic.

Eltner, A., Sardemann, H. & Grundmann, J. (2020) Technical note: flow velocity and discharge measurement in rivers using terrestrial and unmanned-aerial-vehicle imagery. *Hydrology and Earth System Sciences*, 24(3), 1429–1445. Available from: https://doi.org/10.5194/hess-24-1429-2020

Fujita, I., Watanabe, H. & Tsubaki, R. (2007) Development of a non-intrusive and efficient flow monitoring technique: the space-time image velocimetry (STIV). *International Journal of River Basin Management*, 5(2), 105–114. Available from: https://doi.org/10.1080/15715124.2007.9635310

Genç, O., Ardıçlıoğlu, M. & Ağıralioğlu, N. (2015) Calculation of mean velocity and discharge using water surface velocity in small streams. *Flow Measurement and Instrumentation*, 41, 115–120. Available from: https://doi.org/10.1016/j.flowmeasinst.2014.10.013

Hauet, A., Morlot, T. & Daubagnan, L. (2018) Velocity profile and depth-averaged to surface velocity in natural streams: A review over a large sample of rivers. In: *E3S web of Conf*., Vol. 40. Lyon-Villeurbanne, France: EDP Sciences, 06015. Available from: https://doi.org/10.1051/e3sconf/20184006015

Hirvas, H., Lagerback, R., Mäkinen, K., Nenonen, K., Olsen, L., Rodhe, L. & Thoresen, M. (1988) The Nordkalott project: studies of quaternary geology in northern Fennoscandia. *Boreas*, 17(4), 431–437. Available from: https://doi.org/10.1111/j.1502-3885.1988.tb00560.x

Hunter, N.M., Bates, P.D., Horritt, S. & Wilson, M.D. (2007) Simple spatially-distributed models for predicting flood inundation: a review. *Geomorphology*, 90(3-4), 208–225. Available from: https://doi.org/10.1016/j.geomorph.2006.10.021

Hunter, N.M., Bates, P.D., Neelz, S., Pender, G., Villanueva, I.F., Wright, N.G., Liang, D., Falconer, R.A., Lin, B., Waller, S., Crossley, A.J. & Mason, D.C. (2008) Benchmarking 2D hydraulic models for urban flood simulations. *Proceedings of the Institution of Civil Engineers: Water Management*, 161(1), 13–30. Available from: https://doi.org/10.1680/wama.2008.161.1.13

Johnson, E.D. & Cowen, E.A. (2017) Remote determination of the velocity index and mean streamwise velocity profiles. *Water Resources Research*, 53(9), 7521–7535. Available from: https://doi.org/10.1002/2017WR020504

Kasvi, E., Alho, P., Lotsari, E., Wang, Y., Kukko, A., Hyyppä, H. & Hyyppä, J. (2015) Two-dimensional and three-dimensional computational models in hydrodynamic and morphodynamic reconstructions of a river bend: sensitivity and functionality. *Hydrological Processes*, 29(6), 1604–1629. Available from: https://doi.org/10.1002/hyp.10277

Kasvi, E., Salmela, J., Lotsari, E., Kumpula, T. & Lane, S.N. (2019) Comparison of remote sensing based approaches for mapping bathymetry of shallow, clear water rivers. *Geomorphology*, 333, 180–197. Available from: https://doi.org/10.1016/j.geomorph.2019.02.017

Kröhnert, M. & Meichsner, R. (2017) Segmentation of environmental time lapse image sequences for the determination of shore lines captured by hand-held smartphone cameras. *ISPRS Annals of the Photogrammetry, Remote Sensing and Spatial Information Sciences*, IV-2/W4, 1–8. Available from: https://doi.org/10.5194/isprs-annals-IV-2-W4-1-2017

Lane, S., Hardy, R., Ferguson, R. & Parsons, D. (2005) A Framework for Model Verification and Validation of CFD Schemes in Natural Open Channel Flows. In: Bates, P.D., Lane, S.N. & Ferguson, R.I. (Eds.) *Computational fluid dynamics*. Chicester, England: John Wiley & Sons Ltd. Available from: https://doi.org/10.1002/0470015195.ch8

Langhammer, J., Bernsteinová, J. & Miřijovský, J. (2017) Building a high-precision 2D hydrodynamic flood model using UAV photogrammetry and sensor network monitoring. *Watermark*, 9(11), 861. Available from: https://doi.org/10.3390/w9110861

Le Coz, J., Hauet, A., Pierrefeu, G., Dramais, G. & Camenen, B. (2010) Performance of image-based velocimetry (LSPIV) applied to flash-flood discharge measurements in Mediterranean rivers. *Journal of Hydrology*, 394(1-2), 42–52. Available from: https://doi.org/10.1016/j.jhydrol.2010.05.049

Lotsari, E., Calle, M., Benito, G., Kukko, A., Kaartinen, H., Hyyppä, J., Hyyppä, H. & Alho, P. (2018) Topographical change caused by moderate and small floods in a gravel bed ephemeral river - a depth-averaged morphodynamic simulation approach. *Earth Surface Dynamics*, 6(1), 163–185. Available from: https://doi.org/10.5194/esurf-6-163-2018

Lotsari, E., Dietze, M., Kämäri, M., Alho, P. & Kasvi, E. (2020) Macro-turbulent flow and its impacts on sediment transport potential of a Subarctic River during ice-covered and Open-Channel conditions. *Watermark*, 12(7), 1874. Available from: https://doi.org/10.3390/w12071874

Lotsari, E., Hackney, C., Salmela, J., Kasvi, E., Kemp, J., Alho, P. & Darby, S.E. (2020) Sub-arctic river bank dynamics and driving processes during the open-channel flow period. *Earth Surface Processes and Landforms*, 45(5), 1198–1216. Available from: https://doi.org/10.1002/esp.4796

Lotsari, E., Kasvi, E., Kämäri, M. & Alho, P. (2017) The effects of ice-cover on flow characteristics in a subarctic meandering river. *Earth Surface Processes and Landforms*, 42(8), 1195–1212. Available from: https://doi.org/10.1002/esp.4089

Lotsari, E., Tarsa, T., Kämäri, M., Alho, P. & Kasvi, E. (2019) Spatial variation of flow characteristics in a subarctic meandering river in ice-covered and open-channel conditions: 2D hydrodynamic modelling approach. *Earth Surface Processes and Landforms*, 44(8), 1509–1529. Available from: https://doi.org/10.1002/esp.4589

Lotsari, E., Vaaja, M., Flener, C., Kaartinen, H., Kukko, A., Kasvi, E., Hyyppä, H., Hyyppä, J. & Alho, P (2014) Annual bank and point bar morphodynamics of a meandering river determined by high-accuracy multitemporal laser scanning and flow data. *Water Resources Research*, 50(7), 5532–5559.

Lotsari, E., Veijalainen, N., Alho, P. & Käyhkö, J. (2010) Impact of climate change on future discharges and flow characteristics of the tana river, sub-arctic northern Fennoscandinavia. *Geografisca Annaler: Series a, Physical Geograhy*, 92(2), 263–284. Available from: https://doi.org/10.1111/j.1468-0459.2010.00394.x

Lotsari, E., Thorndycraft, V. & Alho, P. (2015) Prospects and challenges of simulating river channel response to future climate change. *Progress in Physical Geography: Earth and Environment*, 39(4), 483–513. Available from: https://doi.org/10.1177/0309133315578944

Lotsari, E., Wang, Y., Kaartinen, H., Jaakkola, A., Kukko, A., Vaaja, M., et al. (2015) Gravel transport by ice in a subarctic river from accurate laser scanning. *Geomorphology*, 246, 113–122. Available from: https://doi.org/10.1016/j.geomorph.2015.06.009

Lucas, B. & Kanade, T. (1981) An iterative image registration technique with an application to stereo vision. In: *Proceedings of the 7th international joint conference on artificial intelligence*. Vancouver, B.C., Canada: University of British Columbia.

Masafu, C., Williams, R., Shi, X., Yuan, Q. & Trigg, M. (2022) Unpiloted aerial vehicle (UAV) image velocimetry for validation of two-dimensional hydraulic model simulations. *Journal of Hydrology*, 612, 128217. Available from: https://doi.org/10.1016/j.jhydrol.2022.128217

Mirauda, D. & Russo, M.G. (2019) Information entropy theory applied to the dip-phenomenon analysis in Open Channel flows. *Entropy*, 21(6), 554. Available from: https://doi.org/10.3390/e21060554

Mirauda, D., Pannone, M. & De Vincenzo, A. (2018) An entropic model for the assessment of streamwise velocity dip in wide open channels. *Entropy*, 20, 69. Available from: https://doi.org/10.3390/e20010069

Moradi, G., Vermeulen, B., Rennie, C.D., Cardot, R. & Lane, S.N. (2019) Evaluation of ADCP processing options for secondary flow identification at river junctions. *Earth Surface Processes and Landforms*, 44(14), 2903–2921. Available from: https://doi.org/10.1002/esp.4719

Morianou, G.G., Kourgialas, N.N. & Karatzas, G.P. (2016) Comparison between curvilinear and rectilinear grid based hydraulic models for river flow simulation. *Procedia Engineering*, 162, 568–575. Available from: https://doi.org/10.1016/j.proeng.2016.11.1022016.11.102

Mosselman, E. (2005) In: Bates, P.D., Lane, S.N. & Ferguson, R.I. (Eds.) *Basic equations for sediment transport in CFD for fluvial Morphodynamics. Computational fluid dynamics: applications in environmental hydraulics*. Chichester, England: John Wiley & Sons Available at: 10.1002/0470015195.ch4.

Mueller, D.S., Wagner, C.R., Rehmel, M.S., Oberg, K.A. & Rainville, F. (2013) Measuring discharge with acoustic Doppler current profilers from a moving boat (USGS Numbered Series No. 3-A22). In: *Surface-water techniques, book 3 applications of hydraulics*. Reston, VA: U.S. Geological Survey Available at: doi.org/10.3133/tm3A22.

Muste, M., Ho, H. & Kim, D. (2011) Considerations on direct stream flow measurements using video imagery: outlook and research needs. *Journal of Hydro-Environment Research*, 5(4), 289–300. Available from: https://doi.org/10.1016/j.jher.2010.11.002

Pappenberger, F., Beven, K., Horritt, M. & Blazkova, S. (2005) Uncertainty in the calibration of effective roughness parameters in HEC-RAS using inundation and downstream level observations. *Journal of Hydrology*, 302(1-4), 46–69. Available from: https://doi.org/10.1016/j.jhydrol.2004.06.036

Polvi, L.E., Dietze, M., Lotsari, E., Turowski, J.M. & Lind, L. (2020) Seismic monitoring of a subarctic river: seasonal variations in hydraulics, sediment transport and ice dynamics. *JGE Earth Surface*, 125(7), e2019JF005333. Available from: https://doi.org/10.1029/2019JF005333

R Core Team. (2022) R: A language and environment for statistical computing (Version 4.2.3) [Software]. R Foundation for Statistical Computing. Available from: https://www.R-project.org/

Rantz, S.E. (1982) Measurement and computation of streamflow. In: *USGS water supply paper, USGS numbered series, 2175*. Washington: U.S. G.P.O.

SonTek. (2013) *RiverSurveyor – discharge, bathymetry and current profiling. S5 and M9 specification sheet*. San Diego, California: Xylem, Inc.

Termini, D. & Moramarco, T. (2018) Dip phenomenon in high-curved turbulent flows and application of entropy theory. *Watermark*, 10(3), 306. Available from: https://doi.org/10.3390/w10030306

Vaaja, M., Hyyppä, J., Kukko, A., Kaartinen, H., Hyyppä, H. & Alho, P. (2011) Mapping topography changes and elevation accuracies using a Mobile laser scanner. *Remote Sensing*, 3(3), 587–600. Available from: https://doi.org/10.3390/rs3030587

Westoby, M.J., Brasington, J., Glasser, N.F., Hambrey, M.J. & Reynolds, J.M. (2012) 'Structure-from-motion' photogrammetry: a low-cost, effective tool for geoscience applications. *Geomorphology*, 179, 300–314. Available from: https://doi.org/10.1016/j.geomorph.2012.08.021

Woodget, A.S., Carbonneau, P.E., Visser, F. & Maddock, I.P. (2014) Quantifying submerged fluvial topography using hyperspatial resolution UAS imagery and structure from motion photogrammetry. *Earth Surface Processes and Landforms*, 40(1), 47–64. Available from: https://doi.org/10.1002/esp.3613

Woodget, A.S., Dietrich, J.T. & Wilson, R.T. (2019) Quantifying below-water fluvial geomorphic change: the implications of refraction correction, water surface elevations, and spatially variable error. *Remote Sensing*, 11(20), 2415. Available from: https://doi.org/10.3390/rs11202415

Wright, K.A., Goodman, D.H., Som, N.A., Alvarez, J., Martin, A. & Hardy, T.B. (2017) Improving hydrodynamic modelling: an analytical framework for assessment of two-dimensional hydrodynamic models. *River Research and Applications*, 33, 170–181. Available from: https://doi.org/10.1002/rra.3067

SUPPORTING INFORMATION

Additional supporting information can be found online in the Supporting Information section at the end of this article.

How to cite this article: Wolff, F., Lotsari, E., Spieler, D., Elias, M. & Eltner, A. (2024) Enhancement of two-dimensional hydrodynamic modelling based on UAV- flow velocity data. *Earth Surface Processes and Landforms*, 49(9), 2736–2750. Available from: https://doi.org/10.1002/esp.5853